Clay Minerals (2023), **58**, 57–66
doi:10.1180/clm.2023.10

CAMBRIDGE UNIVERSITY PRESS

Article

Sintering inhibition and oil-absorption properties of calcined coal-series kaolin

Jiaquan Li[‡], Zhiwei Huang[‡], Qian Wang, Fengnian Zhang, Yang Miao and Feng Gao
College of Material Science and Engineering, Taiyuan University of Technology, Taiyuan, P.R. China

Abstract

In this study, aluminium fluoride trihydrate ($AlF_3{\cdot}3H_2O$) was used to inhibit the sintering of calcined coal-series kaolin (CCSK). In addition, the oil absorption properties of CCSK were studied. The particle-size distribution, specific surface area and porosity of the samples were investigated as a function of calcination temperature and the addition of $AlF_3{\cdot}3H_2O$. Moreover, the ability of $AlF_3{\cdot}3H_2O$ to improve the oil absorption of CCSK was explored. The morphology, structure and phase composition of the specimens were investigated using scanning electron microscopy and X-ray diffraction. The phase transition during heating of the samples was studied using thermogravimetric analysis. The preparation with 10 wt.% $AlF_3{\cdot}3H_2O$ had the optimal sintering inhibition effect on CCSK at 1000°C. The release of SiF_4 gas during heating and the formation of mullite whiskers on the particle surface caused by $AlF_3{\cdot}3H_2O$ moderated the formation of molten-phase liquid bridges between particles and inhibited sintering of the raw material powder. Furthermore, the formation of submicron mullite whiskers on the surface of the CCSK particles enhanced the oil-absorption properties of the sample significantly.

Keywords: $AlF_3{\cdot}3H_2O$, calcined coal-series kaolin, oil absorption, sintering inhibitiom

(Received 14 September 2021; revised 29 March 2023; Accepted Manuscript online: 18 April 2023; editor: George Christidis)

Coal-series kaolin is a product associated with the formation of coal. It is usually greyish-brown in colour and is composed mainly of kaolinite (Xu *et al.*, 2015c; Yuan *et al.*, 2018). With small amounts of impurities, coal-series kaolins have been developed and utilized as important industrial clays with a wide variety of applications in numerous industries, such as the paint, paper, rubber, plastics, ceramics and chemicals industries (Liu *et al.*, 2018; Xie *et al.*, 2019; Muschin *et al.*, 2021). However, the presence of organic matter and coloured minerals in coal-series kaolins reduces the whiteness of the final products, thus decreasing their commercial value (Shelobolina *et al.*, 2005; Huang *et al.*, 2015). To improve the whiteness of coal-series kaolin products, calcination associated with chlorination and some chemical whitening agents has been proposed (González & Ruiz, 2006; Chen *et al.*, 2014). Calcination has a good whitening effect, is low cost and is relatively simple to apply. However, the temperature of the calcination whitening usually reaches 1000°C, causing sintering of the kaolin powder and leading to an increase in the particle size of the powder (Li *et al.*, 2009; Chen *et al.*, 2014; Hernández Chávez *et al.*, 2020). The sintering of calcined coal-series kaolin (CCSK) reduces its value for applications in the paper, paint and rubber industries, which require small powder particle sizes (Dong *et al.*, 2011; El-Sherbiny *et al.*, 2015). Inhibiting the sintering of CCSK is a subject worthy of study.

The main techniques to inhibit particle sintering include particle-coating treatments and the use of additives. Coating particles with thermally stable materials and polymer surface layers prevents sintering during calcination (Okada *et al.*, 2014; Namigata *et al.*, 2020). Wang *et al.* (2014) reduced the sintering tendency of barley straw ash significantly *via* the addition of kaolin and zeolite. Furthermore, the addition of an inert matrix to the raw material may also prevent particle sintering (Mahalingam *et al.*, 2008). However, research focusing on the sintering of CCSK is scarce. The use of additives to inhibit the sintering of CCSK is an efficient and low-cost method compared to particle-coating treatments. Rashad *et al.* (2020) reported that aluminium fluoride trihydrate ($AlF_3{\cdot}3H_2O$) has a greater structural impact on metakaolin particles during calcination. Therefore, $AlF_3{\cdot}3H_2O$ was selected as the sintering inhibitor in this work.

In the paper industry, the oil-absorption value of kaolin is an important factor affecting the quality of coated paper. Kaolin fillers with high oil-absorption values improve the printability of coated paper (Bundy & Ishley, 1991). BASF's Ansilex® 93 (calcined kaolin), produced using weathered kaolin from Georgia, USA, has an oil-absorption value of >90 g 100 g^{-1} (Hen *et al.*, 2000; Khokhani *et al.*, 2019). However, increasing the oil-absorption value of CCSK remains challenging. The coal-series kaolins obtained from coal gangue are usually claystones of sedimentary origin (Ding *et al.*, 2009; Li & Wang, 2019). The kaolinite particles in coal gangue are bound tightly under compaction and cementation. The CCSKs obtained by crushing and calcining the coal gangue do not have the loose particle structure of weathered calcined kaolin, making it difficult to increase the oil-absorption value of CCSKs.

[‡]Contributed equally to this work and should be considered co-first authors
Corresponding author: Yang Miao; Email: miaoyang198781@163.com
Cite this article: Li J, Huang Z, Wang Q, Zhang F, Miao Y, Gao F (2023). Sintering inhibition and oil-absorption properties of calcined coal-series kaolin. *Clay Minerals* **58**, 57–66. https://doi.org/10.1180/clm.2023.10

Table 1. Chemical composition of the coal-series kaolin sample (wt.%).

Sample	SiO_2	Al_2O_3	TiO_2	Fe_2O_3	CaO	MgO	Na_2O	K_2O	Others	LOI
Coal-series kaolin	43.76	37.81	0.81	0.25	0.11	0.10	0.26	0.09	1.10	15.71

LOI = loss on ignition.

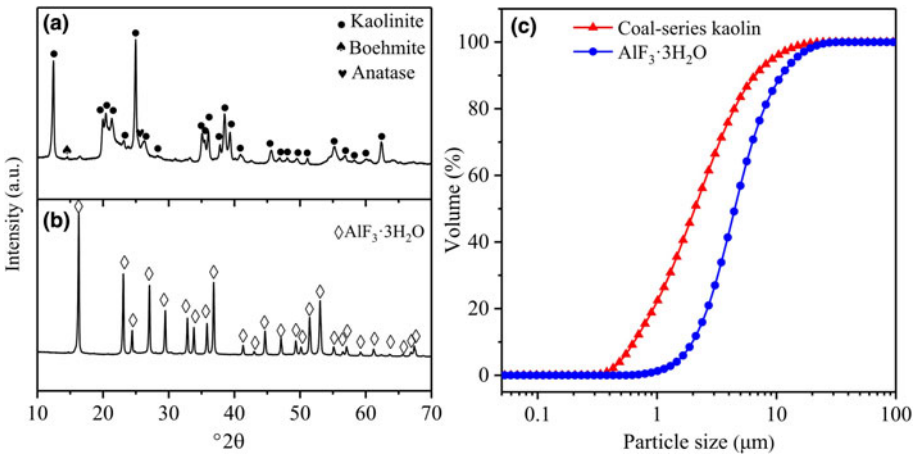

Figure 1. XRD traces of (a) coal-series kaolin and (b) $AlF_3{\cdot}3H_2O$ and (c) cumulative particle-size distribution of raw powder materials.

The purpose of this work is to study the sintering inhibition of CCSK powder by $AlF_3{\cdot}3H_2O$ and to compare the particle-size distribution, microstructure and crystal characteristics of CCSK before and after the addition of $AlF_3{\cdot}3H_2O$. The effects of $AlF_3{\cdot}3H_2O$ addition and temperature on the morphology of calcined kaolin are studied and the oil-absorption properties of CCSK are also investigated.

Experimental

Materials and sample preparation

The CCSK powder was obtained from Shanxi JinKun Mineral Products Co. Ltd (China). The composition of the CCSK samples was determined using X-ray fluorescence (XRF) and the results are listed in Table 1. $AlF_3{\cdot}3H_2O$ powder was supplied by Aladdin Reagent Co. Ltd (China; 98%, CAS 15098-87-0).

The X-ray diffraction (XRD) traces and cumulative particle-size distributions of the raw material powders are shown in Fig. 1. The major mineral of the CCSK sample is kaolinite, associated with minor anatase and boehmite impurities. The particle size of coal-series kaolin is in the range 0.30–27.84 μm, and the cumulative volume frequencies of D_{10}, D_{50} and D_{90} are 0.681, 2.195 and 7.012 μm, respectively. The particle size of $AlF_3{\cdot}3H_2O$ powder is in the range 0.55–35.58 μm, and the cumulative volume frequencies of D_{10}, D_{50} and D_{90} are 2.108, 4.747 and 11.66 μm, respectively.

The $AlF_3{\cdot}3H_2O$ was used as an additive to investigate its effects on the particle-size distribution, microstructure and crystal characteristics of the CCSK during the calcination process. The CCSK and $AlF_3{\cdot}3H_2O$ were mixed at various ratios and stirred with mechanical agitators to achieve thorough mixing. The various mixtures of CCSK and $AlF_3{\cdot}3H_2O$ were labelled KA0, KA2, KA4, KA6, KA8, KA10, KA12 and KA14, corresponding to 0, 2, 4, 6, 8, 10, 12 and 14 wt.% $AlF_3.3H_2O$, respectively. The mixtures were placed in an uncovered alumina crucible and heated to various target temperatures (800, 900 and 1000°C) at a heating rate of 7.5°C min^{-1} for 1 h and cooled in a muffle furnace. The sample 'KA*X*' heated at '*Y*°C' is denoted hereafter as 'KA*X*-*Y*'.

Sample characterization

The chemical composition of the samples was determined using XRF (ARL ADVANT'X Intellipower 3600, USA). The particle-size distributions of sample powders were analyzed using a Mastersizer 3000 laser particle-size analyzer (wet, cycle injection mode and test time of 3 min). The powder XRD traces were recorded in the scanning range of 10–80°2θ using an Ultima IV diffractometer (Rigaku, Japan) operated at 40 kV and 40 mA using Cu-*K*α radiation, with a scanning step of 0.01°2θ and a scanning rate of 5° min^{-1}. Thermogravimetric analysis was performed using an STA 449 F3 simultaneous thermal analyzer (Netzsch, Germany) at 10 K min^{-1} and in an air atmosphere to collect thermogravimetric (TG), derivative thermogravimetric (DTG) and differential scanning calorimetry (DSC) data. The morphology of the samples was observed using scanning electron microscopy (SEM; ZEISS GeminiSEM 300). The N_2 adsorption–desorption isotherms were collected at 77 K using a JWBK122W gas-adsorption device (JWGB Sci. & Tech., China). The specific surface areas were determined using the Brunauer–Emmett–Teller (BET) method and the mesopore-size distribution was obtained based on Barrett–Joyner–Halenda (BJH) analysis of the adsorption branches of the isotherms. Fourier-transform infrared (FTIR) spectra of the samples were obtained using a Nicolet iS5 device (Thermo Fisher Scientific, USA) with KBr discs over the 4000–400 cm^{-1} range. The oil-absorption values of the samples were determined using the Oil Absorption Test (ASTM D281-12, 2021). Detailed information on the instruments and equipment used is listed in Table 2.

Results and discussion

Sintering inhibition of CCSK

During heating, kaolin minerals lose hydroxyls at 450–600°C, forming a disordered-phase, metakaolin (Liu *et al.*, 2015).

https://doi.org/10.1180/clm.2023.10 Published online by Cambridge University Press

Table 2. The main equipment used in the experiment.

Equipment type	Model	Manufacturer
Scanning electron microscope	GeminiSEM 300	Carl Zeiss AG
X-ray diffractometer	Ultima IV	Rigaku Corporation
Specific surface area and aperture analyser	JWBK122W	Beijing JWGB Sci. & Tech. Co., Ltd
Infrared spectrometer	Nicolet iS5	Thermo Fisher Scientific
Particle-size analyser	9300ST	Dandong Baite Technology Co. Ltd
Synchronous thermal analyser	STA 449 F3	NETZSCH-Gerätebau GmbH
Infrared spectrometer	Nicolet iS5	Thermo Fisher Scientific
X-ray fluorescence spectrometer	ARL ADVANT'X	Thermo Fisher Scientific

Metakaolin transforms into a spinel phase at 980°C and mullite is generated as a by-product (Ghorbel *et al.*, 2008; Zhou *et al.*, 2013). The kaolin densification proceeds *via* viscous flux sintering through the formation of an amorphous phase and *via* a diffusion mechanism at the grain boundaries. The alkali and/or iron contents influence the rate at which melting will occur through their fluxing action on silica and alumina (Hernández Chávez *et al.*, 2020). The presence of Fe, Na and K oxides in the kaolin decreases the formation temperature of the molten-phase liquid bridge (Li *et al.*, 2009). In addition, the formation of mullite and spinel phases occurs at the molten-phase liquid bridges as temperature increases. The appearance of liquid bridges in the molten phase and the recrystallization of metakaolin leads to the sintering of the calcined kaolin powder. Therefore, inhibiting the sintering of CCSK is the focus of this work, and the addition of $AlF_3{\cdot}3H_2O$ is proposed as a solution to this problem.

The particle-size distribution, D_{10}, D_{50} and D_{90} values and specific surface areas of CCSK at various temperatures are shown in Fig. 2. The particle-size distribution, particle-size indices and specific surface areas are important performance indicators of powder sintering. The D_{10}, D_{50} and D_{90} values of the samples calcined at 800°C increased significantly when the amount of $AlF_3{\cdot}3H_2O$ was increased from 0 to 14 wt.% (Fig. 2a,b). The reason for this is that the particle size of $AlF_3{\cdot}3H_2O$ is greater than that of KA0-800, and the addition of large particles to small particles increases the mean particle size of the powder. Moreover, the specific surface area increased gradually as the amount of

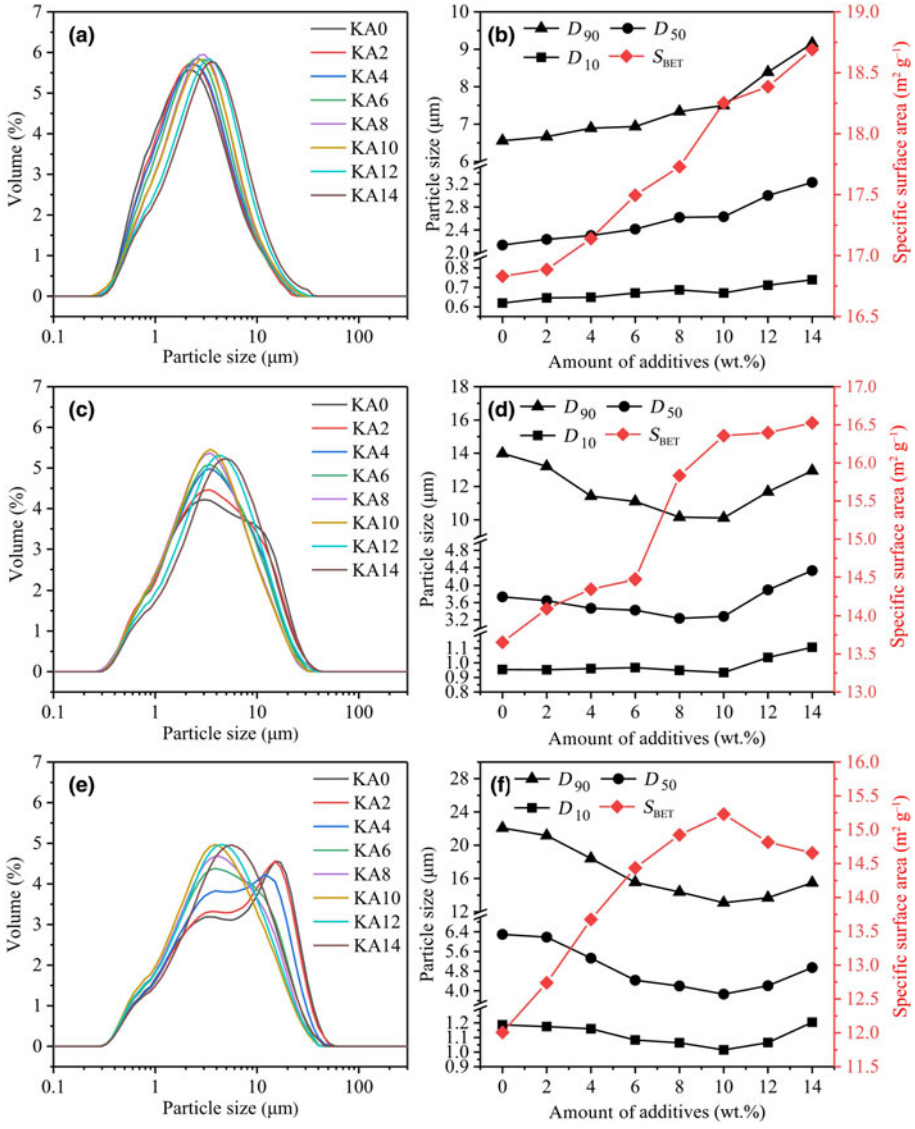

Figure 2. Particle-size distribution, D_{10}, D_{50} and D_{90} values and specific surface area (S_{BET}) of samples at various temperatures: (a,b) 800°C, (c,d) 900°C, (e,f) 1000°C.

https://doi.org/10.1180/clm.2023.10 Published online by Cambridge University Press

$AlF_3·3H_2O$ increased. These changes in particle size and specific surface area indicated that structural transformation had taken place inside the particles due to the reaction of SiO_2 from metakaolin with AlF_3 generated after pyrolysis of $AlF_3·3H_2O$ to produce SiF_4 gas at >600°C, thereby disrupting the structure of metakaolin (Abdel-Rehim, 1999; Moyer & Hughes, 2005; Rashad *et al.*, 2020).

The D_{10}, D_{50} and D_{90} values of the samples calcined at 900°C decreased with increasing $AlF_3·3H_2O$ content from 0 to 10 wt.% (Fig. 2c,d). This could be attributed to the reaction of SiO_2 from metakaolin and AlF_3 to produce SiF_4 gas and topaz. The formed topaz crystals are unstable at >850°C and begin to decompose, releasing SiF_4 gas and forming mullite crystals (Haught *et al.*, 1991; Lee *et al.*, 2008; Abdel-Rehim, 2012). Both reactions moderated the formation of molten-phase liquid bridges between particles and inhibited the sintering of the raw powder material. When the $AlF_3·3H_2O$ content exceeded 10 wt.%, the particle-size indices of the samples increased due to the sintering caused by the formation of a large amount of mullite at the liquid bridges of the molten phases between particles. In addition, the structure of metakaolin was broken and the particle size decreased, so the specific surface area of the sample increased rapidly when the content of $AlF_3·3H_2O$ increased from 0 to 10 wt.%. The particle size of the sample increased with further increases of $AlF_3·3H_2O$ content, but the specific surface area only increased slowly due to the disruption of the structure of metakaolin.

The sample calcined at 1000°C displays a similar trend to the sample calcined at 900°C in terms of the D_{10}, D_{50} and D_{90} values and specific surface area (Fig. 2e,f). The increase in temperature resulted in a greater variation in D_{10}, D_{50} and D_{90} values for the samples calcined at 1000°C. However, the increase in particle size and densification of the powder reduced the specific surface area with further increases in the $AlF_3·3H_2O$ content. In summary, the sintering inhibition effect of $AlF_3·3H_2O$ on CCSK was more obvious at 1000°C. When the $AlF_3·3H_2O$ content was 10 wt.%, the D_{10}, D_{50} and D_{90} values and specific surface area of the sample reached their minimum and maximum values, respectively. Therefore, the following analysis will focus on the effect of $AlF_3·3H_2O$ on CCSK at 1000°C.

The N_2 adsorption–desorption isotherms, pore-size distributions and cumulative pore volumes of four samples are shown in Fig. 3. The isotherms are classified as type II according to the International Union of Pure and Applied Chemistry (IUPAC), indicating macroporous materials. The hysteresis loops of the four samples are related to the capillary condensation of the slit-shaped mesopores in CCSK (Panda *et al.*, 2010; Kuroda *et al.*, 2011). The mode pore diameter of the samples is >50 nm, which is in accordance with that for macroporous materials (Fig. 4a,b). With the addition of increasing amounts of $AlF_3·3H_2O$, the mode pore size first decreased and then increased and the total pore volume increased and then decreased, which is consistent with the sintering law of the sample powders. The decrease in the mode pore size and the increase in the total pore volume are due to the formation of SiF_4 gas, which slows down the sintering densification of the sample, and the formation of a small number of mullite whiskers, which also promotes the development of macropore structures. The increase in the mode pore size and the decrease in the total pore volume in the KA14-1000 sample are due to sintering caused by the growth and production of mullite crystals. The change in the trends of the mode pore size and total pore volume indicate the sintering-inhibitory effect of $AlF_3·3H_2O$ on CCSK.

Sintering-inhibition mechanism of CCSK

The XRD traces of samples containing 10 wt.% $AlF_3·3H_2O$ calcined at various temperatures are shown in Fig. 5a. With increasing temperature, the intensity of the characteristic peak of the kaolinite in the samples decreased gradually until it disappeared due to the destruction of the crystalline structure caused by dehydroxylation (Yan *et al.*, 2017). The mullite peak appeared at 600°C and its intensity increased with increasing temperature. This

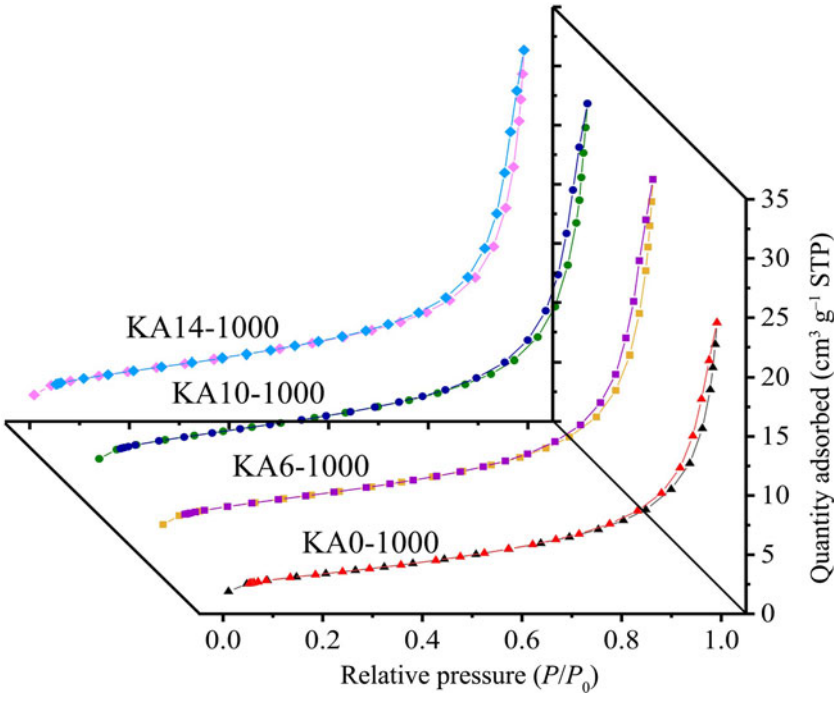

Figure 3. N_2 adsorption–desorption isotherms of the samples. STP = standard temperature and pressure.

https://doi.org/10.1180/clm.2023.10 Published online by Cambridge University Press

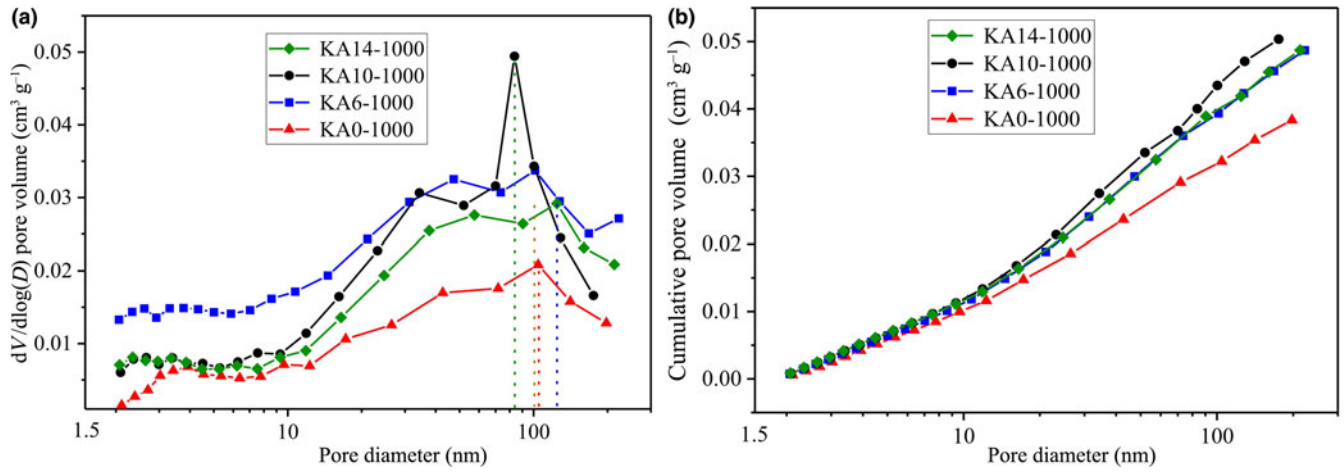

Figure 4. (a) Pore-size distributions and (b) cumulative pore volumes of the samples.

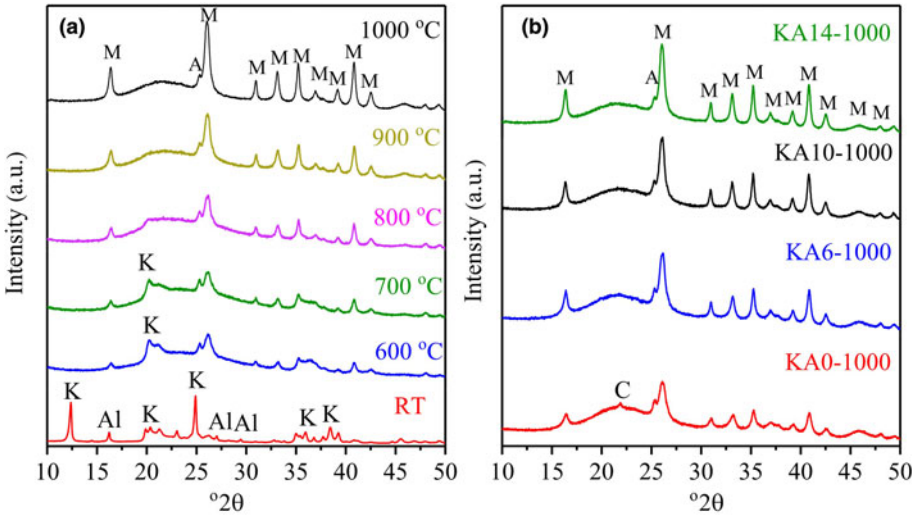

Figure 5. XRD traces of the samples: (a) phase evolution in coal-series kaolin + 10 wt.% $AlF_3·3H_2O$ at various temperatures and (b) calcination of samples with various additions at 1000°C. A = anatase; Al = $AlF_3·3H_2O$; C = cristobalite; K = kaolinite; M = mullite; RT = room temperature.

could be due to the activation of metakaolin and AlF_3 by fluoride ions, which resulted in their reaction, forming a small amount of mullite (Abdel-Rehim, 1999; Bailey *et al.*, 2009). Previous studies have reported the existence of topaz along with minor mullite or sillimanite in the early stages (600–900°C) of sintering (Abdel-Rehim, 2012; Xu *et al.*, 2015a, 2015b). The presence of moisture and HF formed during the reaction can affect topaz nucleation (Rashad *et al.*, 2020). However, the characteristic peaks of AlF_3 and topaz were not observed in the sample after heating to 600°C, which may be due to their low crystal order.

The XRD traces of samples calcined at 1000°C with various quantities of $AlF_3·3H_2O$ are shown in Fig. 5b. In metakaolin, primary mullite begins to appear due to spinel decomposition at ~980°C and increases at greater temperatures, producing excess silica as a glassy phase or cristobalite in the matrix (Chen *et al.*, 2000, 2003; Xu *et al.*, 2015c). The characteristic peaks of cristobalite were observed in the XRD trace of sample KA0-1000. The Al provided by the addition of $AlF_3·3H_2O$ participated in the reaction, forming mullite and excess silica and resulting in the disappearance of the cristobalite in the sample. The main crystalline phase of the sample calcined at 1000°C was mullite (Fig. 5b). Moreover, the characteristic peak intensity of mullite phase increased with increasing $AlF_3·3H_2O$ content, indicating that the mullite content increased gradually. This confirms that the reduction of the D_{10}, D_{50} and D_{90} values is due to the substantial production of mullite.

The results of the TG–DSC–DTG analyses of the CCSK containing 10 wt.% $AlF_3·3H_2O$ are shown in Fig. 6. A major weight loss of 3.94% at 220°C in the mixture corresponds to the removal of molecular water from $AlF_3·3H_2O$ and the moisture being adsorbed in the pores or on the surface of the sample (Xu *et al.*, 2000). The endothermic peak corresponding to the removal of chemically bound water and the formation of AlF_3 from $AlF_3·3H_2O$ was observed at 137°C (corresponding to a DTG peak at 141°C). The small DTG peak at 495°C corresponds to further dehydration and the formation of Al_2O_3 and HF gas (Yang *et al.*, 2007). The main mass loss (13.3%) between 300 and 650°C (corresponding to a DSC endothermic peak at 579°C and a DTG peak at 582°C) is attributed primarily to the formation of metakaolin *via* the dehydroxylation of kaolin. Compared to a previous report on pure kaolin (Zhou *et al.*, 2013), the formation of metakaolin was delayed in time because of the presence of AlF_3 (Rehim, 1979). The DSC curve showed a weak and small endothermic peak at 824°C, corresponding to the release of SiF_4

https://doi.org/10.1180/clm.2023.10 Published online by Cambridge University Press

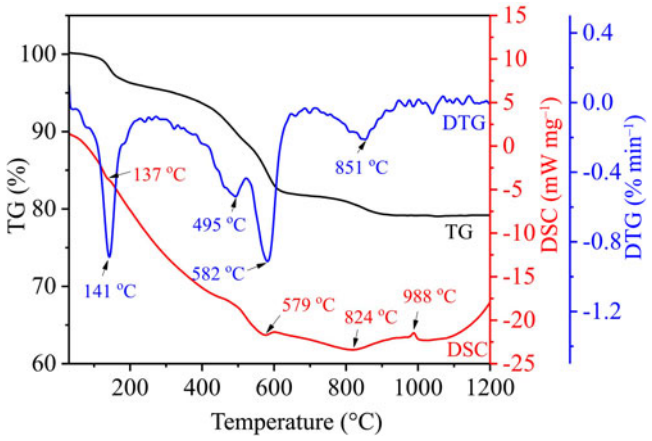

Figure 6. TG–DSC–DTG curves of coal-series kaolin + 10 wt.% $AlF_3 \cdot 3H_2O$.

from topaz (Abdel-Rehim, 2012). In addition, the TG curve exhibited a small weight loss of 2.26 wt.% at 700–950°C (corresponding to a DTG peak at 851°C) due to the high-temperature thermal decomposition of topaz releasing SiF_4 gas. The DSC exothermic peak at 988°C is related to the recrystallization of the amorphous phase and the formation of mullite or a spinel phase.

The SEM images of the samples calcined at 1000°C are shown in Fig. 7. Particles from sample KA0-1000 exhibited lamellar morphology (Fig. 7a,b). However, the structure of kaolin changed from lamellar to amorphous after heating and dehydroxylation, and the XRD data support this interpretation (Zhou *et al.*, 2013; Liu *et al.*, 2017). Therefore, it can be inferred that although the structure of kaolin was still lamellar, it was actually in the process of transformation into an amorphous phase. The particle structure of sample KA0-1000 will be referred to as a 'pseudo-lamellar structure' hereafter. In addition, K_2O and/or Na_2O

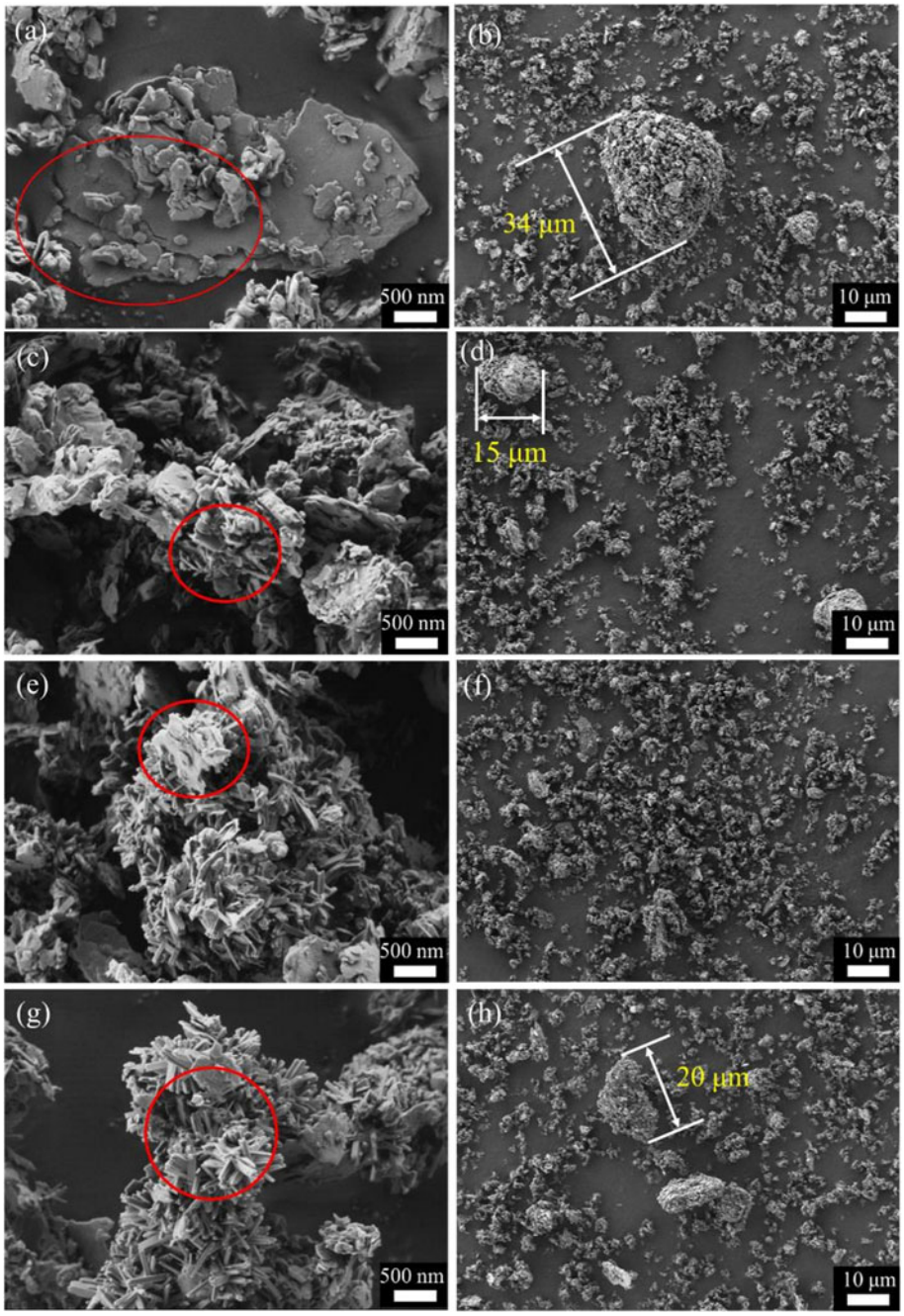

Figure 7. SEM images of CCSK: (a,b) KA0-1000, (c,d) KA6-1000, (e,f) KA10-1000, (g,h) KA14-1000. The red circles highlight features of interest.

https://doi.org/10.1180/clm.2023.10 Published online by Cambridge University Press

decreased the sintering temperature. When the $AlF_3{\cdot}3H_2O$ content increased to 6 wt.%, a small number of mullite whiskers appeared in the disrupted metakaolin sheets (Fig. 7c). The SEM image of sample KA6-1000 (Fig. 7d) shows agglomerated particles with small particle sizes, which is consistent with the results from the particle-size analysis.

A large number of mullite whiskers (~200–400 nm long and 40–80 nm wide) and a small number of disrupted metakaolin sheets appeared on the particle surface in sample KA10-1000 (Fig. 7e). The formation of submicron mullite whiskers on the particle surface and the release of SiF_4 gas disrupted the molten-phase liquid bridges between the particles in the sample, making it difficult for large agglomerated particles to emerge (Fig. 7f). When the $AlF_3{\cdot}3H_2O$ addition reached 14 wt.%, the particle surfaces were covered with mullite whiskers and trace amounts of disrupted metakaolin sheets (Fig. 7g,h). The interweaving of the mullite whiskers resulted in tight binding between small particles, leading to the increase in the particle size observed for sample KA14-1000.

The FTIR spectra of the various samples are presented in Fig. 8. The characteristic bands at 3695, 3651 and 3620 cm^{-1} are attributed to O–H stretching in the CCSK structure (Gong *et al.*, 2018; Zhang *et al.*, 2018). The bands at 1098, 1035 and 917 cm^{-1} correspond to the Si–O stretching vibration, the Si–O–Si symmetric stretching and the Al–OH bending vibration, respectively (Huang *et al.*, 2019). The bands at 755 and 694 cm^{-1} correspond to the Al–OH vibration. The bands at 543, 473 and 432 cm^{-1} correspond to the Si–O–Al, Si–O–Si and Si–O deformations, respectively (Zhang *et al.*, 2014). These bands are typical of kaolinite. When the temperature reached 1000°C, these bands decreased significantly or disappeared, suggesting that the kaolin had dehydroxylated and its structure had been destroyed.

After calcination at 1000°C, the bands of 1098 and 1035 cm^{-1} merged into a single wide band at 1001 cm^{-1}, attributed to Si–O stretching. The new band at 821 cm^{-1} observed after the disappearance of kaolinite is assigned to Al–O stretching of AlO units. In addition, the increase in the $AlF_3{\cdot}3H_2O$ content led to increased substitution of Al for Si, which shifted the band at 821 cm^{-1} (Si *et al.*, 2012). The increase in the mullite content of the calcined sample resulted in an increase in the band intensity of AlO_6 in mullite at 567 cm^{-1} (Percival *et al.*, 2006; Zhou *et al.*, 2013). Finally, the intensity of the Si–O–Si deformation band at 473 cm^{-1} was lessened due to the destruction of the kaolin structure.

By observing the phase evolution and crystal growth of CCSK under various conditions and with reference to the relevant literature, a possible reaction mechanism has been inferred. A rapid escape of water vapour occurred after the decomposition of $AlF_3{\cdot}3H_2O$, starting at 108°C, to AlF_3 (Xu *et al.*, 2000; Stosiek *et al.*, 2008), as per Equation 1:

$$AlF_3 \cdot 3H_2O\ (s) \rightarrow AlF_3(s) + 3H_2O\ (g) \quad (1)$$

The CCSK was transformed to metakaolin by releasing structural water at ~450°C, as per Equation 2:

$$Al_2O_3 \cdot SiO_2 \cdot 2H_2O\ (s) \rightarrow Al_2O_3 \cdot 2SiO_2(s) + 2H_2O\ (g) \quad (2)$$

Along with the removal of structural water from CCSK, the AlF_3 underwent a hydrolysis reaction in the presence of water vapour, generating small quantities of Al_2O_3 and HF (Yang *et al.*, 2007; Stosiek *et al.*, 2008), as per Equation 3:

$$2AlF_3(s) + 3H_2O\ (v) \rightarrow Al_2O_3(s) + 6HF\ (g) \quad (3)$$

The surfaces of the metakaolin and AlF_3 powder were activated significantly in the presence of HF, yielding mullite at ~600°C (Bailey *et al.*, 2009; Xu *et al.*, 2015b), as per Equation 4:

$$aAl_2O_3 \cdot bSiO_2(s) + AlF_3(s) \rightarrow 3Al_2O_3 \cdot 2SiO_2(s) + SiF_4(g) \quad (4)$$

However, the escaping of water vapour and HF activated only a fraction of AlF_3. The remaining AlF_3 was involved mainly in the formation of topaz crystals that began at ~600°C and occurred with intensity at between 770 and 800°C (Rashad *et al.*, 2020),

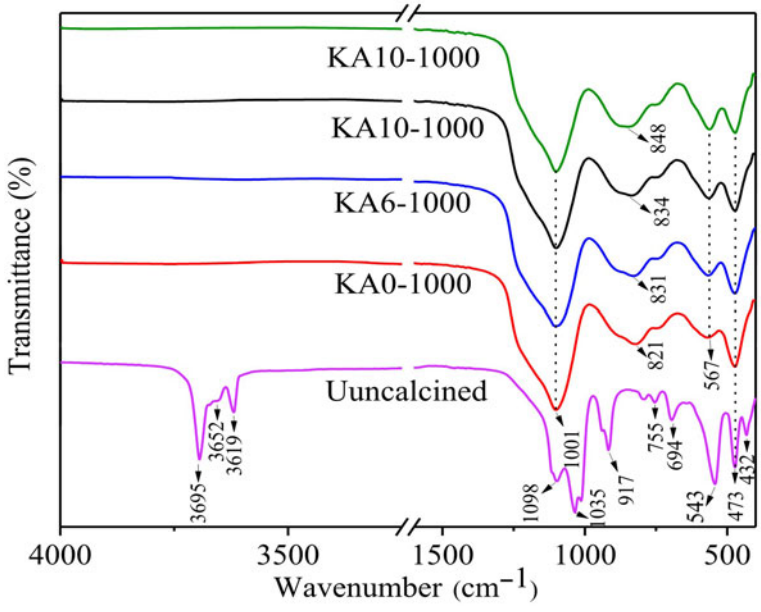

Figure 8. FTIR spectra of uncalcined coal-series kaolin and calcined samples.

https://doi.org/10.1180/clm.2023.10 Published online by Cambridge University Press

Table 3. Changes in the mass of elements before and after calcination of sample KA10-1000 (10 g).

KA10-1000	Si	Al	Ti	Fe	K	Na	Ca	Mg
Before calcination (g)	2.660	1.997	0.086	0.032	0.013	0.012	0.013	0.005
After calcination (g)	2.550	1.997	0.085	0.040	0.013	0.012	0.013	0.006

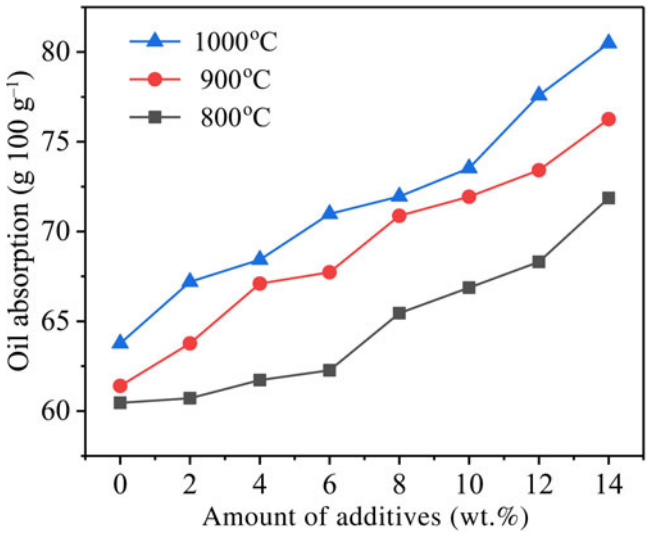

Figure 9. Oil-absorption capacity of CCSK with various additions of $AlF_3{\cdot}3H_2O$.

as per Equation 5:

$$2SiO_2(s) + 2AlF_3(s) \rightarrow Al_2SiO_4F_2(s) + SiF_4(g) \quad (5)$$

The topaz crystals were unstable at >850°C, releasing fluorine upon heating at 850–900°C and forming mullite (Lee *et al.*, 2008; Abdel-Rehim, 2012), as per Equation 6:

$$3Al_2SiO_4F_2(s) + 0.5SiO_2(s) \rightarrow 3Al_2O_3 \cdot 2SiO_2(s) + 1.5SiF_4(g) \quad (6)$$

In metakaolin, primary mullite started to appear due to spinel decomposition at ~980°C and increased at greater temperatures, forming excess silica as a glassy phase or cristobalite in the matrix, as per Equation 7:

$$3(Al_2O_3 \cdot 2SiO_2)(s) \rightarrow 3Al_2O_3 \cdot 2SiO_2(s) + 4SiO_2(s) \quad (7)$$

In summary, CCSK with the addition of $AlF_3{\cdot}3H_2O$ generated great quantities of mullite and SiF_4 gas after calcination. The formation of SiF_4 moderated the formation of molten-phase liquid bridges between particles and inhibited sintering of the raw powder material. Table 3 presents the elemental mass changes of sample KA10-1000 before and after calcination, calculated from XRF data and considering conservation of Al. The amount of Si in the samples decreased after calcination, further suggesting that the release of SiF_4 gas in the system was the main reason for the sintering inhibition of CCSK.

Oil-absorption properties

The oil-absorption values of CCSK with various quantities of added $AlF_3{\cdot}3H_2O$ are shown in Fig. 9. The oil-absorption value of CCSK increased with increasing addition of $AlF_3{\cdot}3H_2O$ at all temperatures, and the oil-absorption value of sample KA14-1000 reached 80.49 g 100 g^{-1}. The oil-absorption models of ordinary particles and 'hedgehog' particles covered with mullite whiskers on their surface are presented in Fig. 10. The absorption of oil by ordinary particles depended mainly on the wetting effect of oil on the particle surface (Fig. 10a,b). The voids formed by the interweaving of mullite whiskers on the surface layers of hedgehog particles could adsorb greater amounts of oil, and the presence of mullite whiskers increased the thickness of the oil layer on the particle surface. Moreover, the thickness of the oil layer between the hedgehog particles was greater than that of ordinary particles at the same particle spacing (Fig. 10c,d), which resulted in the hedgehog particle powders having greater oil-absorption values. Increasing the $AlF_3{\cdot}3H_2O$ content transformed the CCSK particles into hedgehog particles with submicron mullite whiskers on their surfaces (Fig. 7), which increased the oil-adsorption capacity of CCSK. The presence of a large number of mullite whiskers on the particle surface rendered the oil-absorption value of sample KA14-1000 greater than those for all other samples.

A finer and narrower particle-size distribution and an increase in specific surface area increased the oil-absorption value of the calcined kaolin (Hen *et al.*, 2000; Khokhani *et al.*, 2019). When the addition of $AlF_3{\cdot}3H_2O$ exceeded 10 wt.%, the increase in particle size and decrease in specific surface area of the sample calcined at 1000°C did not decrease the oil-absorption value

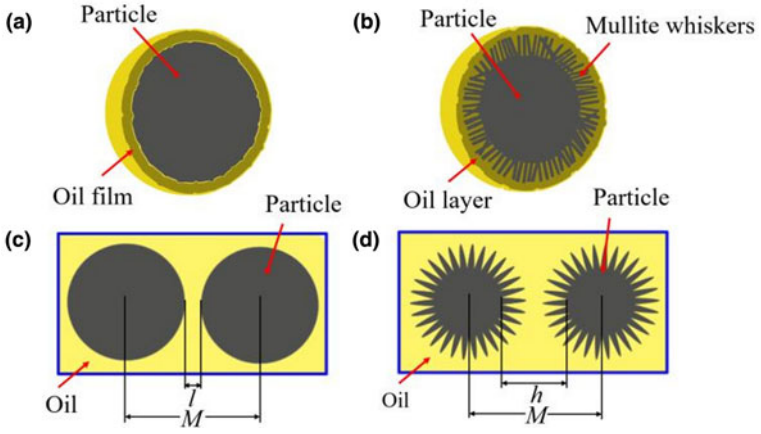

Figure 10. Schematic model describing oil absorption on particles: (a,c) ordinary particles; (b,d) hedgehog particles. *M* refers to particle spacing, whilst *l* and *h* refer to the thickness of the oil layer.

https://doi.org/10.1180/clm.2023.10 Published online by Cambridge University Press

because the significant formation of mullite whiskers on the surfaces of the particles was the main driver underlying the increase in the oil-absorption capacity. Combined with the XRD results, we observe that temperature promoted the formation of mullite whiskers, so the oil-absorption capacity of samples with the same added quantity of $AlF_3{\cdot}3H_2O$ increased with temperature.

Conclusions

The sintering inhibition of CCSK by $AlF_3{\cdot}3H_2O$ was investigated systematically and the oil-absorption capacity of the prepared samples was studied. The main conclusions are as follows:

- The addition of AlF3·3H2O led to a decrease in the D_{10}, D_{50} and D_{90} values and an increase in the specific surface area of the CCSK, suggesting a good sintering-inhibition effect. For the samples calcined at 1000°C, 10 wt.% $AlF_3{\cdot}3H_2O$ produced the best sintering-inhibition effect on CCSK (smallest particle-size indices and greatest specific surface area and total pore volume).
- The release of SiF_4 gas from the sample and the formation of mullite whiskers on the particle surface, caused by $AlF_3{\cdot}3H_2O$, moderated the formation of molten-phase liquid bridges between particles and inhibited the sintering of the raw powder material. However, when $AlF_3{\cdot}3H_2O$ was added in excess, the interweaving of a large number of mullite whiskers led to tight binding between the small particles, resulting in increased particle size in the sample.
- The addition of $AlF_3{\cdot}3H_2O$ improved the oil-absorption capacity of CCSK. The generation of submicron mullite whiskers on the particle surface could improve the oil-absorption value of the sample significantly.

Acknowledgements. We thank the Advanced Inorganic Analysis Laboratory of Taiyuan University of Technology for providing raw materials, experimental equipment and technical guidance.

Financial support. This work is supported by the Science and Technology Major Project of Shanxi Province (20181101004) and Key R&D Project of Shanxi Province (201903D321064).

References

Abdel-Rehim A.M. (1999) Thermal analysis of topaz synthesis from kaolinite. *Thermochimica Acta*, 340–341, 377–386.

Abdel-Rehim A.M. (2012) Thermal and XRD analysis of synthesis of fluoro-topaz. *Thermochimica Acta*, **538**, 29–35.

ASTM D281-12 (2021) *Standard Test Method for Oil Absorption of Pigments by Spatula Rub-out*. ASTM International, West Conshohocken, PA, USA, 2 pp.

Bailey C.L., Mukhopadhyay S., Wander A., Searle B.G. & Harrison N.M. (2009) Structure and stability of α-AlF_3 surfaces. *Journal of Physical Chemistry C*, **113**, 4976–4983.

Bundy W. & Ishley J. (1991) Kaolin in paper filling and coating. *Applied Clay Science*, **5**, 397–420.

Chen C.Y., Lan G.S. & Tuan W.H. (2000) Microstructural evolution of mullite during the sintering of kaolin powder compacts. *Ceramics International*, **26**, 715–720.

Chen Y.F., Wang M.C. & Hon M.H. (2003) Transformation kinetics for mullite in kaolin–Al_2O_3 ceramics. *Journal of Materials Research*, **18**, 1355–1362.

Chen Y.F., Zhou C., Alshameri A., Zhou S., Ma Y., Sun T. *et al.* (2014) Effect of rice hulls additions and calcination conditions on the whiteness of kaolin. *Ceramics International*, **40**, 11751–11758.

Ding S., Liu Q. & Wang M. (2009) Study of kaolinite rock in coal bearing stratum, north China. *Procedia Earth and Planetary Science*, **1**, 1024–1028.

Dong O., Xu W., Lo T.Y. & Sham J.F.C. (2011) Increasing mortar strength with the use of activated kaolin by-products from paper industry. *Construction and Building Materials*, **25**, 1537–1545.

El-Sherbiny S., Morsy F.A., Hassan M.S. & Mohamed H.F. (2015) Enhancing Egyptian kaolinite *via* calcination and dealumination for application in paper coating. *Journal of Coatings Technology and Research*, **12**, 739–749.

Ghorbel A., Fourati M. & Bouaziz J. (2008) Microstructural evolution and phase transformation of different sintered kaolins powder compacts. *Materials Chemistry and Physics*, **112**, 876–885.

Gong B., Ruan B., Zhang Y., Lai X., Yu L., Li Y. & Dang Z. (2018) Differential regulation of phenanthrene biodegradation process by kaolinite and quartz and the underlying mechanism. *Journal of Hazardous Materials*, **349**, 51–59.

González J.A. & Ruiz M.d.C. (2006) Bleaching of kaolins and clays by chlorination of iron and titanium. *Applied Clay Science*, **33**, 219–229.

Haught D., Talmy I., Divecha D. & Karmarkar S. (1991) Mullite whisker felt and its application in composites. *Materials Science and Engineering: A*, **144**, 207–214.

Hen J., Young R., Gines A. & Mathur S. (2000) *Low Sheen Opacifying Pigments and Manufacture Thereof by Calcination of Kaolin Clay*. US Patent No. 613608.

Hernández Chávez M., Vargas Ramírez M., Herrera González A., García Serrano J., Cruz Ramírez A., Romero Serrano J. & Sánchez Alvarado R. (2020) Thermodynamic analysis of the influence of potassium on the thermal behavior of kaolin raw material. *Physicochemical Problems of Mineral Processing*, **57**, 39–52.

Huang T., Lei S., Liu M., Ji M., Liu Y., Yin X. & Peng Y. (2015) Dry separation of iron minerals from low-grade coal-series kaolin. *Journal of Wuhan University of Technology – Materials Science Edition*, **30**, 935–940.

Huang X., Li Y., Yin X., Tian J. & Wu W. (2019) Liquid-phase exfoliation of kaolinite by high-shear mixer with graphite oxide as an amphiphilic dispersant. *Langmuir*, **35**, 13833–13843.

Khokhani A., Yildirim I., Berube R., Mathur S. & Lake A.N. (2019) *Pigment for Paper and Coatings*. US Patent No. 10253186.

Kuroda Y., Ito K., Itabashi K. & Kuroda K. (2011) One-step exfoliation of kaolinites and their transformation into nanoscrolls. *Langmuir*, **27**, 2028–2035.

Lee W.E., Souza G.P., McConville C.J., Tarvornpanich T. & Iqbal Y. (2008) Mullite formation in clays and clay-derived vitreous ceramics. *Journal of the European Ceramic Society*, **28**, 465–471.

Li J. & Wang J. (2019) Comprehensive utilization and environmental risks of coal gangue: a review. *Journal of Cleaner Production*, **239**, 117946.

Li J., Lin H., Li J. & Wu J. (2009) Effects of different potassium salts on the formation of mullite as the only crystal phase in kaolinite. *Journal of the European Ceramic Society*, **29**, 2929–2936.

Liu X., Liu X. & Hu Y. (2015) Investigation of the thermal behaviour and decomposition kinetics of kaolinite. *Clay Minerals*, **50**, 199–209.

Liu Y., Lei S., Lin M., Li Y., Ye Z. & Fan Y. (2017) Assessment of pozzolanic activity of calcined coal-series kaolin. *Applied Clay Science*, **143**, 159–167.

Liu Y., Lei S., Lin M., Xia Z., Pei Z. & Li B. (2018) Influence of calcined coal-series kaolin fineness on properties of cement paste and mortar. *Construction and Building Materials*, **171**, 558–565.

Mahalingam V., Sudarsan V., Munusamy P., van Veggel F.C.J.M., Wang R., Steckl A.J. & Raudsepp M. (2008) Mg^{2+}-doped gan nanoparticles as blue-light emitters: a method to avoid sintering at high temperatures. *Small*, **4**, 105–110.

Moyer J. & Hughes N. (2005) A catalytic process for mullite whiskers. *Journal of the American Ceramic Society*, **77**, 1083–1086.

Muschin T., Zulchin H. & Jia M. (2021) Adsorption behavior of polyhydroxy-iron-modified coal-bearing kaolin for fluoride removal. *ChemistrySelect*, **6**, 3075–3083.

Namigata H., Watanabe K., Okubo S. & Nagao D. (2020) Polymer-coating of photocatalytic particles to prevent sintering in their calcination process. *Colloids and Surfaces A: Physicochemical and Engineering Aspects*, **599**, 124782.

Okada M., Omori Y., Awata M., Shirai T., Matsumoto N., Takeda S. & Furuzono T. (2014) Influence of calcination conditions on dispersibility

https://doi.org/10.1180/clm.2023.10 Published online by Cambridge University Press

and phase composition of hydroxyapatite crystals calcined with anti-sintering agents. *Journal of Nanoparticle Research*, **16**, 2469.

Panda A.K., Mishra B.G., Mishra D.K. & Singh R.K. (2010) Effect of sulphuric acid treatment on the physico-chemical characteristics of kaolin clay. *Colloids and Surfaces A: Physicochemical and Engineering Aspects*, **363**, 98–104.

Percival H., Duncan J. & Foster P. (2006) Interpretation of the kaolinite–mullite reaction sequence from infrared absorption spectra. *Journal of the American Ceramic Society*, **57**, 57–61.

Rashad M., Sabu U., Logesh G., Srishilan C., Lodhe M., Joy A. & Balasubramanian M. (2020) Mullite phase evolution in clay with hydrated or anhydrous AlF_3. *Journal of the European Ceramic Society*, **40**, 5974–5983.

Rehim A.M.A. (1979) Sintering of kaolinite with ammonium fluoride. *Thermochimica Acta*, **30**, 127–139.

Shelobolina E., Pickering S. & Lovley D. (2005) Fe-cycle bacteria from industrial clays mined in Georgia, USA. *Clays and Clay Minerals*, **53**, 580–586.

Si P., Qiao X. & Yu J. (2012) Alumina recovery from kaolin with mineral impurities. *Journal of Wuhan University of Technology – Materials Science Edition*, **27**, 1139–1143.

Stosiek C., Scholz G., Eltanany G., Bertram R. & Kemnitz E. (2008) Novel synthesis and thermal behavior of aluminum hydroxy fluorides $AlF_x(OH)_{3-x}$. *Chemistry of Materials*, **20**, 5687–5697.

Wang L., Skreiberg Ø. & Becidan M. (2014) Investigation of additives for preventing ash fouling and sintering during barley straw combustion. *Applied Thermal Engineering*, **70**, 1262–1269.

Xie X., Niu S., Miao Y., Gao X., Cheng L. & Gao F. (2019) Preparation and properties of resin coated ceramic proppants with ultra light weight and high strength from coal-series kaolin. *Applied Clay Science*, **183**, 105364.

Xu D., Luo Y., Ji Y., Zhou L. & Gai W. (2000) Thermal behavior of aluminum fluoride trihydrate. *Thermochimica Acta*, 352–353, 47–52.

Xu L., Xi X., Shui A. & Zhu W. (2015a) Preparation of mullite whisker skeleton porous ceramic. *Ceramics International*, **41**, 11576–11579.

Xu L., Xi X., Zhu W., Shui A. & Dai W. (2015b) Investigation on the influence factors for preparing mullite-whisker-structured porous ceramic. *Journal of Alloys and Compounds*, **649**, 739–745.

Xu X., Lao X., Wu J., Zhang Y., Xu X. & Li K. (2015c) Microstructural evolution, phase transformation, and variations in physical properties of coal series kaolin powder compact during firing. *Applied Clay Science*, **115**, 76–86.

Yan K., Guo Y., Fang L., Cui L., Cheng F. & Li T. (2017) Decomposition and phase transformation mechanism of kaolinite calcined with sodium carbonate. *Applied Clay Science*, **147**, 90–96.

Yang G.Y., Shi Y.C., Liu X.D. & Mujumdar A.S. (2007) TG–DTG analysis of chemically bound moisture removal of $AlF_3{\cdot}3H_2O$. *Drying Technology*, **25**, 675–680.

Yuan S., Li Y., Han Y. & Gao P. (2018) Effects of carbonaceous matter additives on kinetics, phase and structure evolution of coal-series kaolin during calcination. *Applied Clay Science*, **165**, 124–134.

Zhang Y., Xu L., Seetharaman S., Liu L., Wang X. & Zhang Z. (2014) Effects of chemistry and mineral on structural evolution and chemical reactivity of coal gangue during calcination: towards efficient utilization. *Materials and Structures*, **48**, 2779–2793.

Zhang Q., Yan Z., Ouyang J., Zhang Y., Yang H. & Chen D. (2018) Chemically modified kaolinite nanolayers for the removal of organic pollutants. *Applied Clay Science*, **157**, 283–290.

Zhou H.M., Qiao X. & Yu J.G. (2013) Influences of quartz and muscovite on the formation of mullite from kaolinite. *Applied Clay Science*, 80–81, 176–181.

https://doi.org/10.1180/clm.2023.10 Published online by Cambridge University Press